Pulse Skipping Analysis in Wireless Power Transfer Systems Based on a Reduced-Order Model

Jiayu Zhou, Jiayang Wu, *Member, IEEE*, C. Q. Jiang, *Senior Member, IEEE*, Xiaosheng Wang, Siew-Chong Tan, *Fellow, IEEE*, and Shu-Yuen Ron Hui, *Fellow, IEEE*

***Abstract*—Wireless power transfer (WPT) systems with battery loads exhibit low damping, which results in significant current overshoots and sustained oscillations when subjected to disturbances. Pulse skipping control is frequently employed in WPT systems and can be considered a significant disturbance. However, the accurate analysis of the resulting system dynamics and current envelope remains a challenge. To allow accurate evaluation of the performance of WPT systems with pulse skipping, this article introduces a new reduced-order model for WPT systems through balanced truncation. The derived second-order model enables real-time computation of the current envelopes on both sides of the system, facilitating a comprehensive analysis of the overall performance. This article presents two case studies that utilize this reduced-order model to optimize pulse skipping control in WPT systems. The first study proposes a pulse skipping soft-start strategy based on this model. The second study investigates the optimal pattern of pulse skipping modulations. Simulations and experimental results from a laboratory prototype validate the effectiveness and feasibility of the proposed reduced-order model and the design and refinement of the pulse skipping patterns.**

***Index Terms*—Current stress, pattern refinement, reduced-order model, skipping pulses, soft start-up, wireless power transfer.**

I. Introduction

WIRELESS power transfer (WPT) systems that employ magnetic resonant coupling have attracted significant attention for applications where physical connections are impractical or impossible. This technology holds great promise across multiple applications, ranging from consumer electronics charging to high-power uses in electric vehicles and maritime transport [1], [2], [3], [4]. Among the different compensation topologies, the series–series (SS) configuration with a diode rectifier on the pickup side has proven to be particularly advantageous for certain inductive charging scenarios, such as low-cost applications or high-power demands [4], [5]. This design strikes a balance between system cost, implementation complexity, and power density, making it the preferred choice for battery charging systems that require reliable and efficient power transfer.

The integration of battery loads in wireless charging systems has become increasingly common. While battery loads can be approximated as resistive loads for steady-state analysis [6], [7], this simplification is insufficient for accurately characterizing transient behavior and frequency-domain characteristics due to fundamentally different dynamic models and variations in equivalent resistive load. For transient analysis of battery-loaded systems, a voltage load model is typically employed, since the battery voltage mainly depends on the state of charge and remains stable during short transient intervals [8], [9]. Unlike resistive load systems, battery-loaded systems exhibit notably low damping characteristics, which result in pronounced oscillations when subjected to disturbances [10]. Pulse skipping modulation, commonly encountered in WPT systems, includes techniques such as pulse density modulation [10], [11], [12], [13], [14] and ON–OFF keying modulation [15], [16], [17]. This phenomenon can be regarded as a significant disturbance, leading WPT systems with pulse skipping modulations to exhibit substantial ripples [11] or even oscillations [10]. Optimizing pulse skipping patterns remains a persistent challenge, as conventional solutions often lack detailed analytical models of the system's dynamics, complicating the derivation of pulse patterns that minimize output ripple. While some literature has presented reduced-order models of WPT systems utilizing pulse skipping modulations and their corresponding envelopes [12], [13], these analyses typically assume constant resistive loads. This approach is fundamentally different from the dynamic models of WPT systems with voltage loads, leading to variations in system order and corresponding envelopes that cannot be equivalently transformed.

To analyze system dynamics and design effective controllers, a dynamic model is essential. Although the transient model can be numerically processed to evaluate dynamic characteristics [18], it offers limited insight into the phase and current envelope of the dynamic system. To address the discontinuities and time-varying nature of the transient model and derive an analytical solution, dynamic models of WPT systems based on dynamic phasor transformation [19], generalized steady-state averaging

Received 4 June 2025; revised 23 September 2025; accepted 16 October 2025. Date of publication 23 October 2025; date of current version 19 January 2026. This work was supported in part by Hong Kong RGC General Research Fund under Grant 172120025 and in part by Hong Kong RGC Theme-based Research Project under Grant T23-708/24-N. Recommended for publication by Associate Editor A. Safaee. *(Corresponding author: Jiayang Wu.)*

Jiayu Zhou, Jiayang Wu, C. Q. Jiang, Xiaosheng Wang, and Siew-Chong Tan are with the Department of Electrical Engineering, City University of Hong Kong, Hong Kong (e-mail: jiayzhou@cityu.edu.hk; jiayang.wu@cityu.edu.hk; chjiang@cityu.edu.hk; xiaoswang9-c@my.cityu.edu.hk; siewctan@cityu.edu.hk).

Shu-Yuen Ron Hui is with the Department of Electrical Engineering, City University of Hong Kong, Hong Kong, and also with the Department of Electrical and Electronics Engineering, Imperial College London, SW7 2BX London, U.K. (e-mail: eeronhui@cityu.edu.hk).

Color versions of one or more figures in this article are available at https://doi.org/10.1109/TPEL.2025.3624876.

Digital Object Identifier 10.1109/TPEL.2025.3624876

[20], [21], and extended describing functions [22] have been proposed. In WPT systems, the fundamental harmonics approximation (FHA) is often employed to simplify analysis. With FHA, nonlinear model equations derived from these methods remain consistent while maintaining high accuracy. Essentially, the oscillating state variable (ac signal) can be transformed into two slowly varying variables (approximate dc signals) using the Fourier series transformation, typically yielding system orders of 8 or 9 (with 9 accounting for the dc side filter capacitance and resistive load). However, the high system order complicates the derivation of analytical solutions for current envelopes, which are critical for analyzing pulse skipping. Several reduced-order models have been proposed to analyze the dynamic behavior of the system. In [23], the *s*-domain approximation reduces the system order to 5. Polynomial approximation methods presented in [24] allow for reductions to orders of 1, 3, or 5. Additionally, energy balancing techniques reported in [25] have been used to establish a reduced-order dynamic model. Despite these efforts, the aforementioned reduced-order approaches still face significant challenges. Specifically, obtaining analytical solutions for models of order three or higher remains computationally intractable [23], [24], [25], thereby precluding a detailed analysis of the pulse-skipping phenomenon. While simplifying the system to a first- or second-order model yields analytical expressions, the resulting accuracy is insufficient to reliably characterize the current envelope during pulse skipping [24]. Consequently, an accurate analytical formulation for the current envelope at any given instant, which is essential for effective pulse-skipping refinement, remains elusive.

To comprehensively analyze pulse skipping, this article presents a balanced truncation-based model order reduction technique that effectively simplifies the original eighth-order system into a second-order model. The analytical expressions for the current envelopes on both sides of the system are fully developed, enabling high-accuracy analysis of the system's dynamic behavior. To support our study, two case studies of different application scenarios are adopted to illustrate the model's application in analyzing and refining pulse skipping patterns. First, the reduced-order model is utilized to first analyze the startup process, and then to develop a rapid pulse-skipping soft-start method for the WPT system. Low-damped WPT systems often exhibit overshoot and oscillations during startup. Traditionally, soft starting has been achieved through techniques such as phase shift modulation that can compromise zero-voltage switching (ZVS) [17], or pulse frequency modulation [26] that may lead to power overshoot in systems exhibiting frequency-splitting phenomena [27]. In this study, a pulse skipping strategy is proposed to achieve soft starting while maintaining ZVS. The derived reduced-order model and current envelope are adopted to assist the design of the proposed soft starting method. Second, the derived model enables an accurate analysis of current ripples in WPT systems using pulse skipping modulation. This provides insights into refining pulse patterns to minimize output current/power ripples. Moreover, the reduced-order model proves valuable for various applications, including dynamic performance analysis and the development of model-based control strategies. The effectiveness of the proposed model and methods is validated through simulation studies and experimental verification.

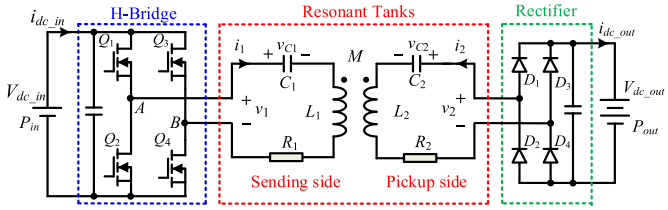

Fig. 1. SS-compensated IPT system with a voltage load.

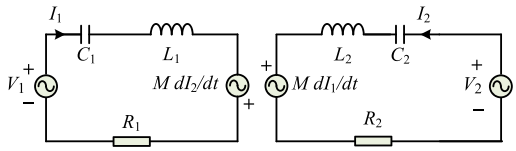

Fig. 2. Equivalent circuit of the SS-compensated IPT system with a voltage load using first harmonic approximation.

II. System Nonlinear Modeling of SS-Compensated IPT Systems With Voltage Load

Fig. 1 depicts a traditional SS-compensated WPT system. In this setup, the variables v_1 (v_2), i_1 (i_2), L_1 (L_2), C_1 (C_2), and R_1 (R_2) denote the sending-side (pickup-side) voltage, current, inductance, capacitance, and series equivalent resistances, respectively. M represents the mutual inductance between the coils. Additionally, the system's output is connected to a battery load. In millisecond-level transient analyses, it is standard practice to model the battery as a voltage load [8], [9], [10], [17]. It is worth noting that a typical battery model features a small internal resistance in series with its open-circuit voltage. Given its very small value, which has a negligible effect on the system dynamics, this internal resistance is not considered in the present model [10], [17]. Fundamentally, this resistance can be conceptually mapped to the ac pickup side. Therefore, the proposed model remains valid without structural change; the only potential effect is a minor increase in the value of the existing resistance R_2, representing the sum of the original ac internal resistance and the mapped battery's internal resistance. The system is typically operated at the resonant frequency ($\omega_r = 1/\sqrt{L_1C_1} = 1/\sqrt{L_2C_2}$) to minimize reactive power, particularly when employing pulse skipping. Applying the FHA, both v_1 and v_2 are considered sinusoidal waveforms. The equivalent circuit for the system is illustrated in Fig. 2. When the output of the diode rectifier is linked to a voltage load, the relationship between the ac-side pickup voltage/current and the resulting dc output voltage can be described as follows [8]:

$$\begin{cases} |V_2| = \frac{4}{\pi} V_{\mathrm{dc,out}} \\ \angle V_2 = -\angle I_2. \end{cases} \tag{1}$$

Moreover, the time-varying ac signal states can be transformed into dc signals with real and imaginary components

using the *dq* synchronous reference frame

$$x_{idq} = x_{id} + jx_{iq}. \tag{2}$$

Based on the equivalent circuit shown in Fig. 2 and the relationships defined in (1) and (2), the corresponding nonlinear model with a voltage load can be expressed in the state-space form [21]. This form, as given in (3), accurately represents the system's dynamic behavior and enables a deeper understanding of its characteristics

$$\begin{cases} \dot{\boldsymbol{x}} = f(x,u) \\ y = g(x,u) \end{cases} \tag{3}$$

with the state $\boldsymbol{x}$, input signal $\boldsymbol{u}$ and output signal $\boldsymbol{y}$ defined by

$$\boldsymbol{x} = [i_{1d} \quad i_{1q} \quad i_{2d} \quad i_{2q} \quad v_{C1d} \quad v_{C1q} \quad v_{C2d} \quad v_{C2q}]^T$$
$$\boldsymbol{u} = [v_{1d} \quad v_{1q} \quad \omega \quad V_{\text{dc-out}}]^T$$
$$\boldsymbol{y} = [I_1 \quad P_{\text{in}}]^T.$$

The resulting nonlinear state-space model of the presented IPT system from Fig. 2 is expressed by the following eight equations [10], [21]:

$$(a)\frac{di_{1,d}}{dt} = \omega \cdot i_{1,q} - \frac{R_1}{L_{\alpha1}} \cdot i_{1,d} + \frac{MR_2}{L_{\alpha1}L_2} \cdot i_{2,d} - \frac{1}{L_{\alpha1}} \cdot v_{C1,d} + \frac{M}{L_{\alpha1}L_2} \cdot v_{C2,d} + \frac{1}{L_{\alpha1}} \cdot v_{1,d} + \frac{M}{L_{\alpha1}L_2} \cdot \frac{i_{2,d}}{\sqrt{i_{2,d}^2 + i_{2,q}^2}} \cdot \frac{4}{\pi} \cdot V_{\text{dc\_out}}$$

$$(b)\frac{di_{1,q}}{dt} = -\omega \cdot i_{1,d} - \frac{R_1}{L_{\alpha1}} \cdot i_{1,q} + \frac{MR_2}{L_{\alpha1}L_2} \cdot i_{2,q} - \frac{1}{L_{\alpha1}} \cdot v_{C1,q} + \frac{M}{L_{\alpha1}L_2} \cdot v_{C2,q} + \frac{1}{L_{\alpha1}} \cdot v_{1,q} + \frac{M}{L_{\alpha1}L_2} \cdot \frac{i_{2,q}}{\sqrt{i_{2,d}^2 + i_{2,q}^2}} \cdot \frac{4}{\pi} \cdot V_{\text{dc\_out}}$$

$$(c)\frac{di_{2,d}}{dt} = \omega \cdot i_{2,q} + \frac{MR_1}{L_{\alpha2}L_1} \cdot i_{1,d} - \frac{R_2}{L_{\alpha2}} \cdot i_{2,d} + \frac{M}{L_{\alpha2}L_1} \cdot v_{C1,d} - \frac{1}{L_{\alpha2}} \cdot v_{C2,d} - \frac{M}{L_{\alpha2}L_1} \cdot v_{1,d} - \frac{1}{L_{\alpha2}} \cdot \frac{i_{2,d}}{\sqrt{i_{2,d}^2 + i_{2,q}^2}} \cdot \frac{4}{\pi} \cdot V_{\text{dc\_out}}$$

$$(d)\frac{di_{2,q}}{dt} = -\omega \cdot i_{2,d} + \frac{MR_1}{L_{\alpha2}L_1} \cdot i_{1,q} - \frac{R_2}{L_{\alpha2}} \cdot i_{2,q} + \frac{M}{L_{\alpha2}L_1} \cdot v_{C1,q} - \frac{1}{L_{\alpha2}} \cdot v_{C2,q} - \frac{M}{L_{\alpha2}L_1} \cdot v_{1,q} - \frac{1}{L_{\alpha2}} \cdot \frac{i_{2,q}}{\sqrt{i_{2,d}^2 + i_{2,q}^2}} \cdot \frac{4}{\pi} \cdot V_{\text{dc\_out}}$$

$$(e)\frac{dv_{c1,d}}{dt} = \omega \cdot v_{c1,q} - \frac{1}{C_1} \cdot i_{1,d}$$

$$(f)\frac{dv_{c1,q}}{dt} = -\omega \cdot v_{c1,d} + \frac{1}{C_1} \cdot i_{1,q}$$

$$(g)\frac{dv_{c2,d}}{dt} = \omega \cdot v_{c2,q} + \frac{1}{C_2} \cdot i_{2,d}$$

$$(h)\frac{dv_{c2,q}}{dt} = -\omega \cdot v_{c2,d} + \frac{1}{C_2} \cdot i_{2,q} \tag{4}$$

where $L_{\alpha1} = L_1 - M^2/L_2$, and $L_{\alpha2} = L_2 - M^2/L_1$. Moreover, the magnitudes of the sending and pickup currents in the system can be determined using the following equation:

$$\begin{cases} I_1 = \sqrt{i_{1d}^2 + i_{1q}^2} \\ P_{\text{in}} = v_{1d} \cdot i_{1d} + v_{1q} \cdot i_{1q} = v_{1d} \cdot i_{1d}. \end{cases} \tag{5}$$

By simultaneously solving (1)–(5), the full-order nonlinear model can derive the entire system state and output quantities when the input quantities are known. Therefore, it can be stated that knowing only the four quantities in $\boldsymbol{u}$ is sufficient to determine all quantities in $\boldsymbol{x}$ and $\boldsymbol{y}$. Based on the parameters listed in Table I, the transient current amplitude during the system startup process is calculated, as illustrated by the dark red line in Fig. 3. Additionally, the blue curve in Fig. 3 represents the time-domain response of the system's sending current, obtained through the circuit model in MATLAB/Simulink. The results demonstrate that the full-order model in (3) accurately captures the system's transient response, aligning closely with the circuit results. During startup, both the sending and pickup currents experience overcurrent conditions, with their amplitudes reaching approximately twice the rated value. This results in prolonged oscillations due to the system's low damping characteristics. This phenomenon also leads to a doubling of the voltage across the resonant capacitors. Consequently, WPT systems with a voltage load are susceptible to overcurrent and overvoltage conditions in their components during startup, increasing the likelihood of failures. Consequently, WPT systems with a voltage load are

TABLE I
PARAMETERS OF THE IPT-SYSTEM

General parameters	Values
Input dc voltage, $V_{\text{dc\_in}}$	24 V
Output battery voltage, $V_{\text{dc\_out}}$	24 V
Coupling coefficient, k	0.05–0.35
Resonant frequency, f_r	85.0 kHz
Self-inductance, L_1, L_2	42, 42 μH
Quality factor, Q_1, Q_2	280, 280

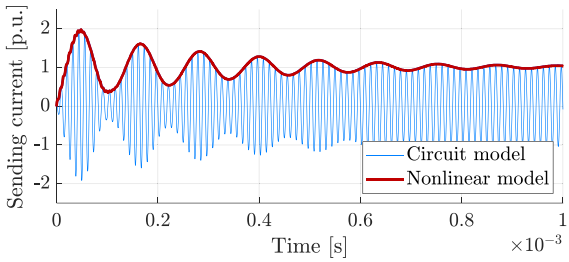

Fig. 3. Sending current obtained from the full-order nonlinear model and the circuit model of the WPT system during the startup process.

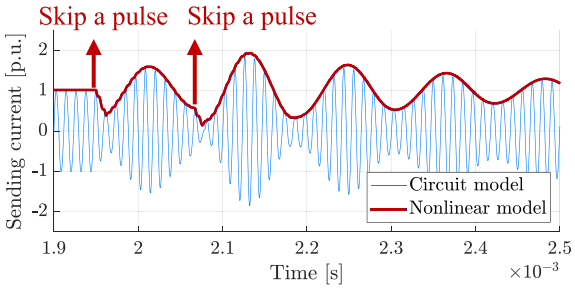

Fig. 4. Sending current obtained from the full-order nonlinear model and the circuit model of the WPT system with pulse skipping modulations.

prone to overcurrent and overvoltage conditions during startup, which increases the likelihood of component failures. Analyzing the startup process using a full-order model presents challenges, as a detailed analytical solution is often unattainable.

Pulse-skipping modulation is also prevalent in WPT systems. Fig. 4 presents the results obtained from the full-order nonlinear model as indicated by the dark red line, alongside the actual circuit simulation results that are represented by the blue line. The consistency between the nonlinear model and the circuit simulation results is evident. Additionally, Fig. 4 illustrates the oscillations of pulse skipping that was originally reported in [10]. When the frequency of the skipped pulse aligns with the system's natural frequency, it can induce oscillations. Therefore, determining the optimal timing for pulse skipping, which is essentially a process of refining the pulse patterns, presents a significant challenge in WPT systems.

Both of these issues necessitate a comprehensive analysis of the current envelope model, which is complicated by the complexities inherent in the higher-order transfer functions outlined in (3) and (4). Thus, it is essential to consider effective order reduction techniques to facilitate the analysis of the current model and the design of pulse-skipping strategies.

III. Reduced Model Based on Balanced Truncation

The nonlinear dynamic model has been developed using the generalized state-space averaging method. However, the oscillating state variables in this model are transformed into dc signals comprising both real and imaginary components, effectively doubling the order of the nonlinear model. The complexity of this eight-order system renders analytical modeling cumbersome, limiting insights into the system's dynamic behaviors. Moreover, high-order systems significantly increase the challenges and computational demands that are associated with model-based control. Therefore, a reduced-order model is essential for simplifying dynamic analysis and calculating the current envelope. This reduction facilitates the implementation and refinement of pulse-skipping techniques in various scenarios.

First, the nonlinear system shown in (3) should be linearized at the steady-state point $(\boldsymbol{x_0}, \boldsymbol{u_0})$ at the resonant frequency ω_r. This process results in the following system:

$$\begin{cases} \Delta\dot{\boldsymbol{x}} = \boldsymbol{A}\left(\boldsymbol{x}_0, \boldsymbol{u}_0\right)\Delta\boldsymbol{x} + \boldsymbol{B}\left(\boldsymbol{x}_0, \boldsymbol{u}_0\right)\Delta\boldsymbol{u} \\ \Delta\boldsymbol{y} = \boldsymbol{C}\left(\boldsymbol{x}_0, \boldsymbol{u}_0\right)\Delta\boldsymbol{x} + \boldsymbol{D}\left(\boldsymbol{x}_0, \boldsymbol{u}_0\right)\cdot\Delta\boldsymbol{u} \end{cases}. \tag{6}$$

The Jacobian matrices **A**, **B**, **C,** and **D** can be easily obtained by differentiating (4), as documented in [10]. Consider the system model in (6) with controllability and observability Gramians W_c and W_o. They are symmetric, positive semidefinite matrices that satisfy certain relationships

$$\begin{cases} \boldsymbol{A}W_c + W_c\boldsymbol{A}^T + \boldsymbol{B}\boldsymbol{B}^T = 0 \\ \boldsymbol{A}^T W_o + W_o\boldsymbol{A} + \boldsymbol{C}^T\boldsymbol{C} = 0. \end{cases} \tag{7}$$

To truncate states that are difficult to reach and observe, a balancing transformation is employed. This involves a state-space transformation using an invertible matrix $\boldsymbol{T} \in \mathbb{R}^{n\times n}$ to create a transformed system

$$\begin{cases} \dot{\boldsymbol{x}} = \boldsymbol{T}^{-1}\boldsymbol{A}\boldsymbol{T}\cdot\boldsymbol{x} + \boldsymbol{T}^{-1}\boldsymbol{B}\cdot\boldsymbol{u} \\ \boldsymbol{y} = \boldsymbol{C}\boldsymbol{T}\cdot\boldsymbol{x} + \boldsymbol{D}\cdot\boldsymbol{u} \end{cases}. \tag{8}$$

Under this transformation, the Gramians evolve as

$$\bar{W}_c = \boldsymbol{T}W_c\boldsymbol{T}^{\boldsymbol{T}}\bar{W}_o = \boldsymbol{T}^{-\mathbf{T}}W_o\boldsymbol{T}^{-\mathbf{1}}. \tag{9}$$

The transformed system is referred to as a balanced realization when its transformed Gramians satisfy $\bar{W}_c = \bar{W}_o = \mathrm{diag}(\sigma_1, \sigma_2, \sigma_3, \cdots \sigma_n)$, is a diagonal positive definite matrix. The diagonal entries σ_i, known as Hankel Singular Values (HSVs), are computed as given in [28]

$$\sigma_i = \sqrt{\lambda_i(W_cW_o)}(i = 1, 2, \cdots, 8) \tag{10}$$

where λ_i denotes the ith eigenvalue of the product W_cW_o. Controllability can be viewed as the amount of input "energy" required to drive the system from the zero state to a specific state $\boldsymbol{x}$. Observability, on the other hand, reflects how much "energy" is contained in the output response starting from a certain initial state $\boldsymbol{x}$ without any input applied. If a state is easily excited (strongly controllable) and produces a significant output response (strongly observable), its HSV σ_i will be large. This indicates that it serves as an "efficient channel" for transferring energy between input and output, making it crucial for understanding input–output behavior. Each HSV reflects the "energy" contribution of its corresponding state to the system's input–output behavior, serving as a quantitative measure of the state's influence on the overall dynamics of the system. Balanced truncation is a robust method that generates a lower-order approximation of the model by systematically neglecting states with relatively low impact on the dynamic response. By utilizing lower-order approximations that preserve essential dynamic characteristics, this approach facilitates simplified analysis and control design. Specifically, retaining high-energy states ensures that key system attributes, such as stability, frequency response, and time dynamics, are maintained.

The HSVs of the full-order detailed model can be computed, as illustrated in Fig. 5. The top two states (i_{1d}, i_{1q}) exhibit significant singular values, indicating their substantial impact on system behavior. Conversely, states with low magnitudes can be excluded, allowing for the construction of a reduced-order model that does not compromise critical dynamic information. From a physical standpoint, the sending-side current (i_{1d}, i_{1q}) primarily determines the strength and quality of the magnetic field among the eight state variables. In contrast, the pickup-side

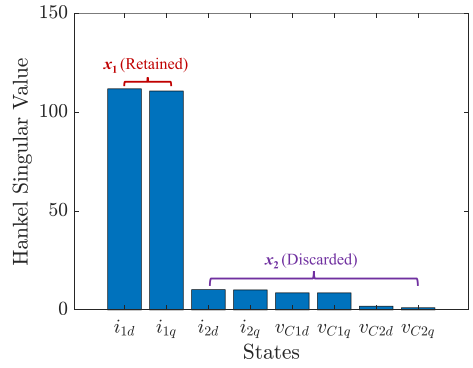

Fig. 5. Hankel singular values of the full-order model.

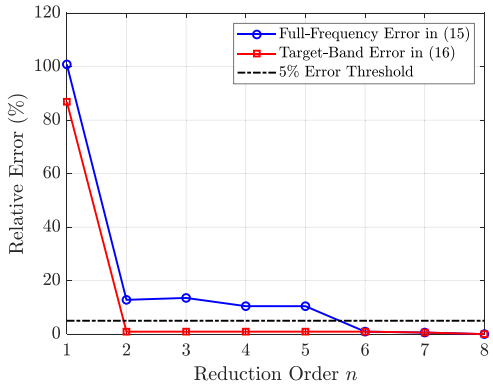

Fig. 6. Errors of the full-order model and various reduced-order models based on balanced truncation.

currents ($i_{2\,d}$, $i_{2\,q}$) are more passive, influenced by the sending-side current, while $v_{C1(2)\,d}$ and $v_{C1(2)\,q}$ depend entirely on $i_{1(2)\,d}$ and $i_{1(2)\,q}$. Therefore, the sending-side current exhibits high controllability and observability, resulting in larger HSVs and dominance in the system.

Upon balancing the system, a partition of the realization must first be obtained to facilitate the computation of the reduced system [29]

$$\begin{cases} \dot{\boldsymbol{x}}_1 = \boldsymbol{A}_{11} \cdot \boldsymbol{x}_1 + \boldsymbol{A}_{12} \cdot \boldsymbol{x}_2 + \boldsymbol{B}_1 \cdot \boldsymbol{u} \\ \dot{\boldsymbol{x}}_2 = \boldsymbol{A}_{21} \cdot \boldsymbol{x}_1 + \boldsymbol{A}_{22} \cdot \boldsymbol{x}_2 + \boldsymbol{B}_2 \cdot \boldsymbol{u} \\ \boldsymbol{y} = \boldsymbol{C}_1 \cdot \boldsymbol{x}_1 + \boldsymbol{C}_2 \cdot \boldsymbol{x}_2 + \boldsymbol{D} \cdot \boldsymbol{u} \end{cases} \tag{11}$$

where "slow states" $\boldsymbol{x_1} \in \mathbb{R}^r$ and "fast states" $\boldsymbol{x_2} \in \mathbb{R}^{n-r}$.

By employing balanced truncation in conjunction with singular perturbation approximation, which is a method that effectively reduces the order of the system by setting the derivatives of the fast states to zero, the reduced system and its corresponding transfer function can be derived as [29], [30]

$$\begin{cases} \dot{\mathbf{x}}_1 = \boldsymbol{A_r} \cdot \boldsymbol{x}_1 + \boldsymbol{B_r} \cdot \boldsymbol{u} \\ \boldsymbol{y} = \boldsymbol{C_r} \cdot \boldsymbol{x}_1 + \boldsymbol{D_r} \cdot \boldsymbol{u} \end{cases} \tag{12}$$

where $\boldsymbol{A_r}=\boldsymbol{A_{11}}-\boldsymbol{A_{12}}\boldsymbol{A_{22}^{-1}}\boldsymbol{A_{21}}; \boldsymbol{B_r}=\boldsymbol{B_1}-\boldsymbol{A_{12}}\boldsymbol{A_{22}^{-1}}\boldsymbol{B_2}$
$\boldsymbol{C_r}=\boldsymbol{C_1}-\boldsymbol{C_2}\boldsymbol{A_{22}^{-1}}\boldsymbol{A_{21}}; \boldsymbol{D_r}=\mathbf{D}-\boldsymbol{C_2}\boldsymbol{A_{22}^{-1}}\boldsymbol{B_2}$.

By applying the Laplace transformation to both sides of the state equation presented in (12), the following results are obtained:

$$\begin{cases} X_1(s) = (sI - \boldsymbol{A_r})^{-1}\boldsymbol{B_r}U(s) \\ Y(s) = \boldsymbol{C_r}[(sI - \boldsymbol{A_r})^{-1}\boldsymbol{B_r}U(s)] + \boldsymbol{D_r}U(s). \end{cases} \tag{13}$$

Simplifying (13) allows for the derivation of the system's transfer function

$$G_r(s) = \frac{Y(s)}{U(s)} = \boldsymbol{C_r}(sI - \boldsymbol{A_r})^{-1}\boldsymbol{B_r} + \boldsymbol{D_r}. \tag{14}$$

At this stage, the order reduction system has been completed, which can effectively analyze the sending/pickup side current envelope with high precision. The subsequent evaluation focuses on the accuracy of the explanatory model. First, the global error between the reduced-order system $G_r(s)$ and the full-order system $G(s)$ is defined as follows:

$$\gamma_1 = \|G(s) - G_r(s)\|_\infty = \sup_{\omega\in\mathbb{R}} \overline{\sigma}(G(j\omega) - G_r(j\omega)). \tag{15}$$

However, for the current amplitude under investigation, the primary components do not include high-frequency content, such as the resonant frequency. Instead, these components predominantly consist of dc elements and the system's natural frequency, which typically ranges from one twentieth to one fifth of the switching frequency; the exact value depends on the coupling coefficient.

Consequently, during the order reduction process, attention shifts from the global error to the error within the frequency range from dc to three times the natural frequency (ω_n). In this context, the error of the reduced-order model within this frequency band can be articulated as

$$\gamma_2 = \sup_{\omega\in[0,3\omega_n]} \overline{\sigma}(G(j\omega) - G_r(j\omega)) \le \varepsilon_2. \tag{16}$$

In the current envelope analysis presented herein, achieving high accuracy within a specified frequency range is generally considered adequate. Therefore, the objective is to maintain an error of less than 5% within this specified frequency range for the reduced-order model, thereby ensuring an accurate analysis of the system's current envelope.

Fig. 6 illustrates the error between the actual system and various reduced-order systems when the coupling coefficient is 0.2. It is evident that for system orders ranging from 2 to 8, the error remains significantly below 5% within the specified frequency range. As a result, the system can be effectively reduced to a second-order model, facilitating the attainment of an analytical solution and enabling real-time analysis of the current envelope.

By simultaneously solving (6) to (14), the transfer function of the second-order system can be derived. This enables further dynamic analysis of pulse skipping in WPT systems. Two case study examples are introduced in the following. Section IV presents the proposed pulse-skipping soft-start strategy based on the derived model. Section V demonstrates how pulse-skipping modulation is refined to minimize current ripples.

IV. Proposed Soft Start Strategy Using Pulse Skipping Control Based on the Reduced-Order Model

The preceding analysis indicates that the SS-compensated WPT system with a voltage load can be effectively reduced into

a second-order system that is characterized by extremely low damping. This configuration inherently produces significant current oscillations during startup, necessitating the use of oversized components to prevent system failure. Therefore, implementing a soft-start mechanism is essential for WPT systems. To facilitate a rapid soft start, this article proposes a pulse-skipping method based on the presented reduced-order model. This approach not only ensures a smooth startup process, but also maintains ZVS, thereby mitigating EMI issues associated with hard switching. This section outlines the specific design scheme based on the reduced-order model, along with detailed simulation results.

A. Startup Analysis Based on Reduced-Order Model

Based on the derived reduced-order model, the entire system's startup process can be accurately analyzed, facilitating the design of a soft-start mechanism. However, during the initial startup phase, the reduced-order model obtained from Fig. 2 cannot be directly used. Unlike systems with resistive loads, WPT systems featuring battery loads initially operate solely on the sending side during startup, as there is no current present on the pickup side at that moment. The diode rectifier becomes operational during startup only when the sending current satisfies the following condition:

$$\omega_r M I_1(t) > \frac{4}{\pi} V_{\text{dc\_out}} = V_2. \tag{17}$$

Before the condition outlined in (17) is satisfied, the system operates exclusively on the sending side, which consists of the H-bridge output voltage and an LC circuit. When the system operates at its resonant frequency, it can be accurately modeled as a first-order system [17]. In this context, the envelope function of the sending current can be calculated as follows:

$$I_1(t) = \frac{V_1}{R_1}\left(1 - e^{-\frac{R}{2L_1}t}\right). \tag{18}$$

Based on (17) and (18), the time required for the transition from startup to the initiation of conduction on the pickup side can be calculated as follows:

$$t_1 = -\frac{2L_1}{R_1}\text{In}\left(1 - \frac{R_1 V_2}{\omega_r M V_1}\right). \tag{19}$$

After t_1, the diode rectifier on the pickup side begins operation, and the system's working mode is illustrated in Fig. 2. At this stage, by employing the equivalent simplified circuit analysis in [23] alongside the reduced-order model result in (14), the calculation of the current envelope can be expressed as follows:

$$I_1(t) \approx e^{-\zeta\omega_n(t-t_1)}\left[\left(I_{10} - \frac{V_2}{\omega_r M}\right)\cos(\omega_d(t-t_1)) + \frac{\sqrt{L_2/L_1}(V_1 - \omega_r M I_{20})}{\omega_r M}\sin(\omega_d(t-t_1))\right] + \frac{V_2}{\omega_r M} \tag{20}$$

$$I_2(t) \approx e^{-\zeta\omega_n(t-t_1)}\left[\sqrt{L_1/L_2}\left(I_{10} - \frac{V_2}{\omega_r M}\right)\sin(\omega_d(t-t_1)) - \frac{(V_1 - \omega_r M I_{20})}{\omega_r M}\cos(\omega_d(t-t_1))\right] + \frac{V_1}{\omega_r M} \tag{21}$$

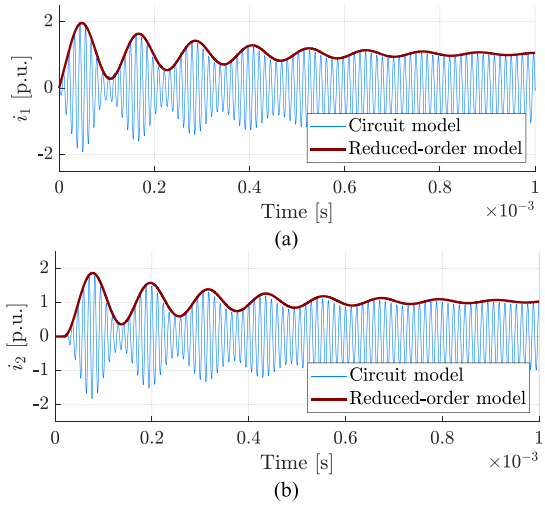

Fig. 7. (a) Sending current and (b) pickup current obtained from the reduced-order model and the circuit model of the WPT system during startup.

where I_{10} and I_{20} represent the current amplitudes of the sending side and the pickup side at time t_1, respectively. ζ and ω_n are the damping ratio and natural frequency of the second-order system, respectively. ω_d is the damping frequency of the system and can be calculated as $\omega_d = \sqrt{\omega_n^2 - \zeta^2}$. These parameters can be directly obtained by (14).

Fig. 7 displays the corresponding simulation results, where the blue line represents the time-domain waveform obtained from the circuit model, while the red line illustrates the envelope of the current amplitude that is calculated using the reduced-order model from (18)–(21). It is evident that the presented model derived from balanced truncation exhibits high accuracy, making it suitable for designing a soft-start mechanism. Although some existing literatures have derived their current envelope equations using reduced first or second-order models for soft start [17], [31], these results obtained are based on certain simplifications and have not been compared or validated against circuit models. Furthermore, since current fluctuations and frequent interference must be considered in real time, the use of a high-precision reduced-order model for pulse skipping control design is essential. In this article, verification demonstrates that the current envelope equation from the reduced second-order model closely matches the actual circuit model, will be provided.

B. Soft-Start Design Using Pulse-Skipping Based on Reduced-Order Model

For the startup of low-damped WPT systems, designing a fast soft-start method is crucial. Additionally, achieving ZVS during this process is essential to avoid high voltage spikes and EMI issues. To address these challenges, a pulse-skipping method is proposed to facilitate a fast soft start while maintaining ZVS throughout the process. This section focuses on the design of

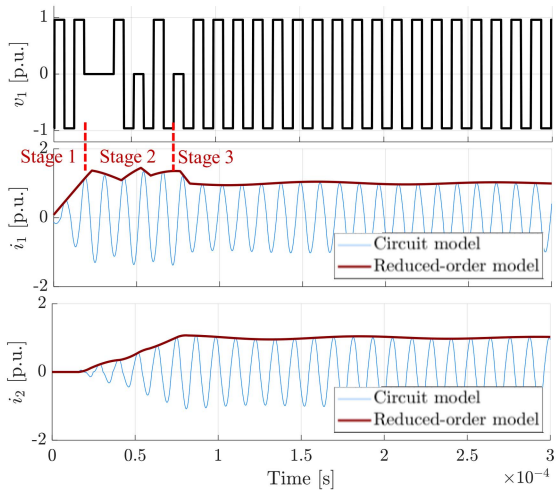

Fig. 8. Designed soft start process of the WPT system with voltage load based on the reduced-order model.

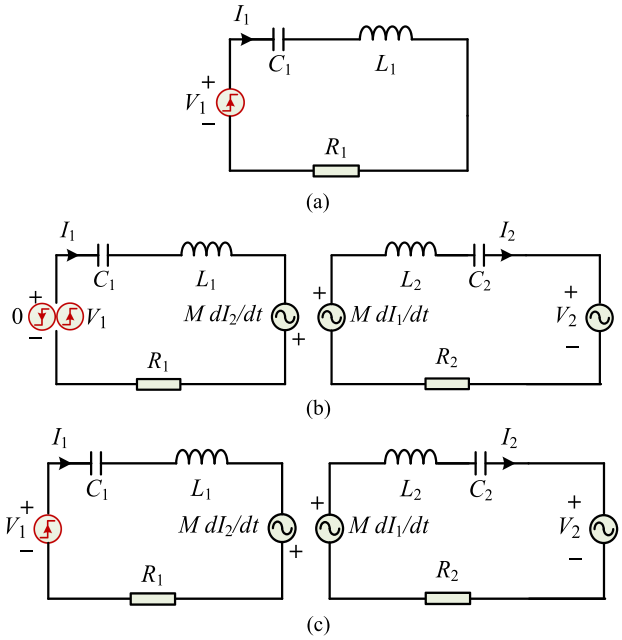

Fig. 9. Equivalent circuit of the designed soft start process for the WPT system. (a) Stage 1 for I_1 increase. (b) Stage 2 for I_2 smooth increase. (c) Stage 3 for fast stabilization.

the pulse-skipping modulation to achieve a soft start, based on the previously developed reduced-order model.

The entire soft-start process can be divided into three stages, with the corresponding simulation results shown in Fig. 8. The process concludes within approximately 1.5 ms, at which point both the sending-side and pickup-side currents reach steady state. Soft-switching is maintained throughout the startup transient, with only a minor overshoot exhibited by the sending-side current. The first stage involves the initiation of I_1, which corresponds to the sending-side LC resonance process represented by (18) and (19). Fig. 9(a) illustrates the equivalent circuit diagram of this process, representing a second-order LC circuit operating at the resonant frequency. This allows I_1 to increase rapidly until the pickup-side diode rectifier becomes operational, following the conditions outlined in (18). This process has been previously analyzed and will not be reiterated here. Once the rectifier on the pickup side activates, the system transitions to the second stage. If the system does not utilize a soft start, it will begin to oscillate at the damping frequency, as shown in Fig. 7. In contrast, in the designed soft-start process, I_2 should gradually increase during this stage, as depicted in Fig. 8, while I_1 is maintained as close to the rated current as possible.

The equivalent circuit at stage 2 is shown in Fig. 9(b), where the equivalent output voltage of the sending-side H-bridge switches between 0 and V_1, representing the pulse-skipping process. It is important to note that the system's operating frequency remains unchanged, corresponding to the resonant frequency. This means that the system can only eliminate pulses at the rising or falling edges of the input pulses. Consequently, when I_1 exceeds 1.1 times its rated value, the next pulse should be skipped in the designed soft-start method. This process can be conceptualized as V_1 stepping down to 0. At this point, the envelopes of the currents on the sending and pickup sides can be obtained and are shown as follows:

$$I_1(t) \approx e^{-\zeta\omega_n(t-t_0)}\left[\left(I_{10}-\frac{V_2}{\omega_r M}\right)\cos(\omega_d(t-t_0)) - \sqrt{L_2/L_1}I_{20}\sin(\omega_d(t-t_0))\right]+\frac{V_2}{\omega_r M} \tag{22}$$

$$I_2(t) \approx e^{-\zeta\omega_n(t-t_0)}\left[\frac{\sqrt{L_1/L_2}\left(I_{10}-\frac{V_2}{\omega_r M}\right)}{\omega_r M}\sin(\omega_d(t-t_0)) - I_{20}\cos(\omega_d(t-t_0))\right] \tag{23}$$

where I_{10} and I_{20} represent the current amplitudes on the sending and pickup sides at the initial moment of the skipped pulse. Equations (20)–(23) can be utilized to determine the pulses that ought to be skipped. Analyzing the current envelope equations reveals that an increase in I_1 beyond the rated value leads to a rise in I_2, while a decrease in I_1 results in a reduction of I_2. By calculating how many cycles I_1 remain below the rated value, it can be determined when to turn the pulse back on to allow I_1 to rise. Through iterative calculations, the necessary cycles to be skipped in stage 2 are identified until I_2 reaches the rated value. At this point, stage 3 needs to be introduced. Although I_2 has increased to the rated value, the system is still oscillating, as indicated by (20) to (23). To mitigate this effect, the simplest approach is to skip one pulse at this moment and allow v_1 to step from 0 to V_1, as illustrated in Fig. 9(c). Calculations show that when I_2 reaches the rated value and v_1 steps from 0 to the rated value, the final fluctuations in the system are quickly suppressed in stage 3, allowing the current to stabilize at the rated value, as illustrated in the simulation shown in Fig. 8. Additionally, the results of the reduced-order model based on (17)–(23) are presented in Fig. 8 as indicated by the red line, demonstrating a high degree of consistency with the circuit model. This congruence supports its use in designing the entire soft-start process. Based on the presented reduced-order model,

the startup process of the entire system has been successfully designed by implementing pulse skipping, completing the soft start within 15 switching cycles (less than 0.2 ms). Throughout this process, the system consistently achieved ZVS.

V. Pattern Refinement for Pulse Skipping Modulation Based on the Reduced-Order Model

The reduced-order model of the WPT system with a voltage load, along with the corresponding current envelope, has been derived and utilized to design the proposed pulse-skipping soft-start system in the previous section. Specifically, (20)–(23) can be directly employed to analyze the current ripples when the system experiences pulse skipping. In this section, a second case study based on the reduced-order model is presented, focusing on refining the pulse-skipping modulation pattern to minimize current/power ripples. Pulse-skipping modulation is a widely used technique in WPT systems as it allows operation at the resonant frequency while achieving ZVS across the entire power range [10], [11], [12], [13], [14], [15], [16], [17]. However, a significant challenge faced by existing WPT systems utilizing pulse skipping modulation is the potential for large current ripple [11] or even oscillation [10]. One common solution involves adding virtual damping [10] [17], although this loses ZVS. Another approach focuses on refining the output pattern [12], [13], [14], which can substantially reduce current/power ripples while maintaining ZVS. It is important to note that reference [12], [13] refines the output pattern based on the derived model and current envelope for WPT systems with resistive loads, making it inapplicable to typical systems with voltage loads due to their distinct dynamic characteristics [10]. Additionally, while the study in [14] offers pattern refinement based on voltage loads, it lacks theoretical support or system model analysis. Therefore, leveraging on the reduced-order model derived in this article, including (14) and (20)–(23), the results for a refined output pattern can be derived.

Pulse skipping consists of two distinct phases. Initially, the voltage drops to zero and remains at this level for one switching cycle before rising back to its rated value. Consequently, when the system skips a pulse, the current amplitude on the primary side follows (22) during the skipped switching cycle, then transitions to (20). Similarly, the secondary side operates according to (23) for one switching cycle before switching to (21). It can be observed that the current amplitudes on both sides initially drop and then rise, continuing to oscillate briefly in the absence of additional disturbances. Therefore, the strategy for triggering the next skipped pulse to minimize output ripples warrants discussion. Based on (21), it can be established that when I_1 and I_2 reach their rated values at the rising edge of the skipped pulse, the pickup current amplitude becomes smooth, minimizing the ripples

$$I_2(t)\big|_{I_{10}(t_0)\approx\frac{V_2}{\omega_r M};I_{20}(t_0)=\frac{V_1}{\omega_r M}} \approx e^{-\zeta\omega_n(t-t_0)} \times \left[\sqrt{L_1/L_2}\left(I_{10}-\frac{V_2}{\omega_r M}\right)\sin(\omega_d(t-t_0)) - \frac{(V_1-\omega_r M I_{20})}{\omega_r M}\cos(\omega_d(t-t_0))\right] + \frac{V_1}{\omega_r M} \approx \frac{V_1}{\omega_r M}. \quad (24)$$

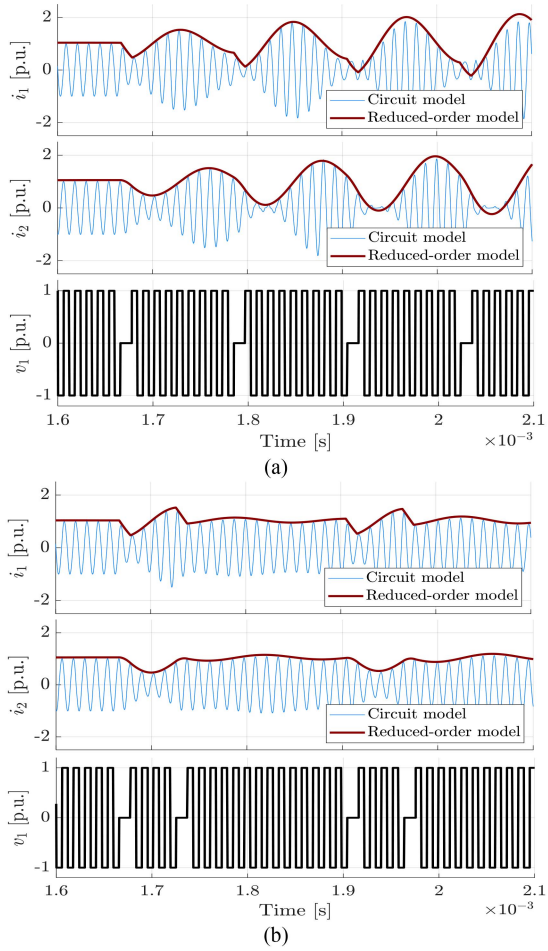

Fig. 10. Simulation results of pulse skipping modulations with different output patterns ($k = 0.2$; $d = 0.90$). (a) Average pulse skipping modulation. (b) Optimized pattern based on reduced-order model.

However, it is generally challenging to attain both conditions simultaneously due to the phase difference between the oscillation components of I_1 and I_2. Analysis of (20)–(23) reveals that I_2 lags behind I_1. As I_2 rises from below the rated value to the rated value, I_1 usually decreases from above the rated value to the rated value. Therefore, skipping a pulse when I_2 rises and approaches the rated value is the most effective strategy for closely satisfying the conditions in (24). Fig. 10 illustrates the simulation results of two pulse skipping methods for WPT systems with a pulse density (d) of 0.9 and coupling coefficient (k) of 0.2. Fig. 10(a) presents the results of an average skipped pulse when the frequency of the skipped pulse aligns with the system's natural frequency [10]. This configuration can lead to significantly large current oscillation on both the sending and pickup sides. By refining the output pattern as informed by (24) and the preceding analysis, the simulation results are depicted in

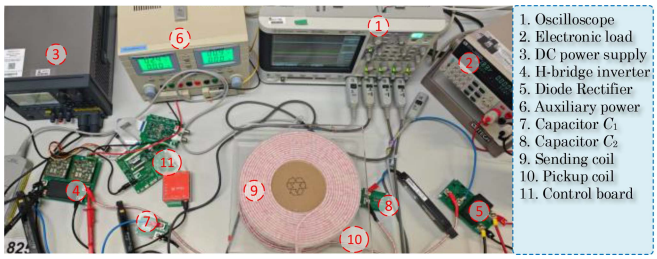

Fig. 11. Prototype of the WPT system for experimental verification.

Fig. 10(b). As discussed, the skipped pulse pattern is observed when I_2 rises and approaches the rated value. The findings indicate that adopting this optimized pattern enables the system to achieve a smooth output rapidly, thereby minimizing output current ripples. These results serve as a preliminary example of pattern refinement that can be extended to more generalized solutions. Notably, substantial current ripples, as illustrated in Fig. 10(a), typically occur only at high pulse densities, suggesting opportunities for pattern refinement through the proposed method. When the pulse density falls below 0.7, the system tends to skip pulses frequently, complicating the application of insights derived from (24). However, in these scenarios, the system generally exhibits low ripple levels. With increased damping and frequent pulse skipping, the system struggles to oscillate at its natural frequency [10], thereby diminishing the necessity for pulse refinement. Thus, the conventional average skipped pulse can be effectively utilized.

VI. Experimental Results

To validate the proposed reduced-order model, soft-start technique, and pulse-skipping pattern refinement method, experimental tests were conducted using the laboratory prototype illustrated in Fig. 11, which is constructed according to the parameters detailed in Table I. The system operates at an input voltage of 24 V, with a power rating of 85 W. The inverter employs a GaN MOSFET, specifically the EPC 2071 model, and is driven by the uP1966E gate driver. The diodes used on the receiving side are SBM3060VDCAU_R2_006A1. The input side of the prototype is connected to a dc voltage source, while the output side is linked to an electronic load operating in constant voltage mode to emulate a battery.

Fig. 12 presents the experimental results of the system when it is operating in steady state, and is suddenly made to skip a single pulse. Here, oscillations in both sending and pickup currents can be observed after the introduction of the pulse. Utilizing the reduced-order model defined by (20)–(23), the current envelopes were calculated, and a comparison with the experimental results demonstrates a high degree of accuracy. This validates the effectiveness of the reduced-order model.

Fig. 13 shows the experimental results of the system's direct startup process, including waveforms of it sending voltage, sending current, dc side current, and pickup current. Significant and prolonged oscillations of the resulting waveforms can be observed. Notably, the amplitude of the oscillating current exceeds 9 A, which is approximately twice the rated current. This poses a considerable challenge for system design. Additionally, the results calculated using the reduced-order model are also presented in Fig. 13. Due to the complexity of the startup (dynamic) process and variations in parasitic parameters, the calculated results are less accurate compared to those obtained for the system when skipping a pulse, as shown in Fig. 12. Nevertheless, the results in Fig. 13 illustrate that the oscillation frequency aligns closely with a small amplitude error. Essentially, this slight inaccuracy has a negligible impact on the subsequent soft-start design for pulse skipping.

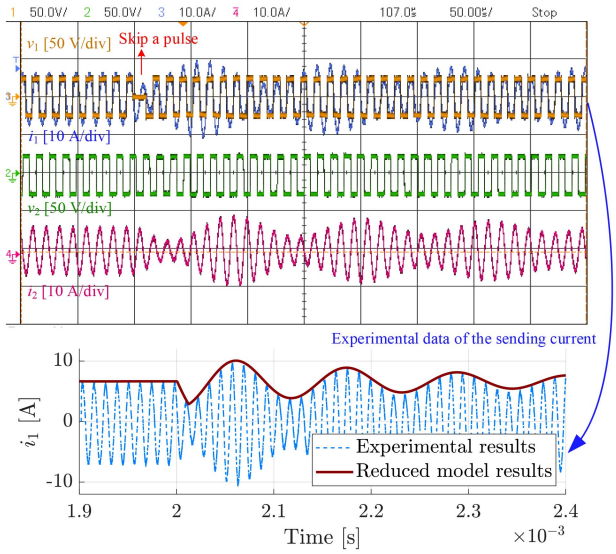

Fig. 12. Experimental results and calculated results from the reduced-order model when the system skips a single pulse.

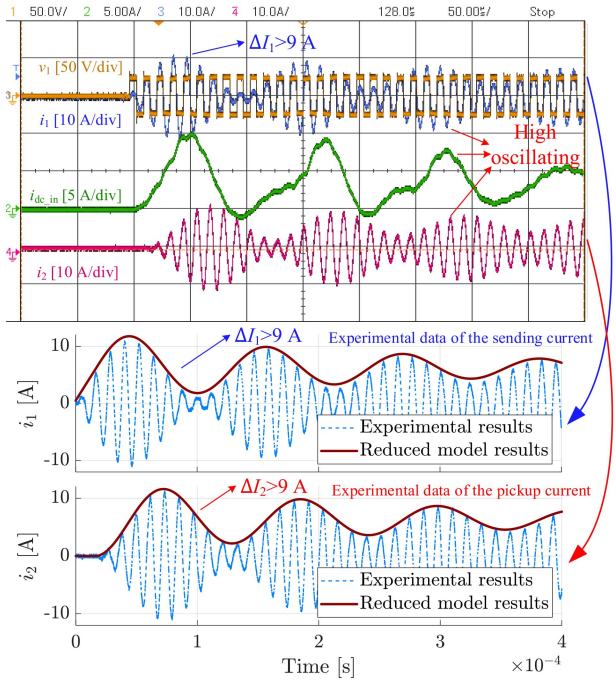

Fig. 13. Experimental results and calculated results from the reduced-order model for direct startup of the WPT system with $k = 0.22$.

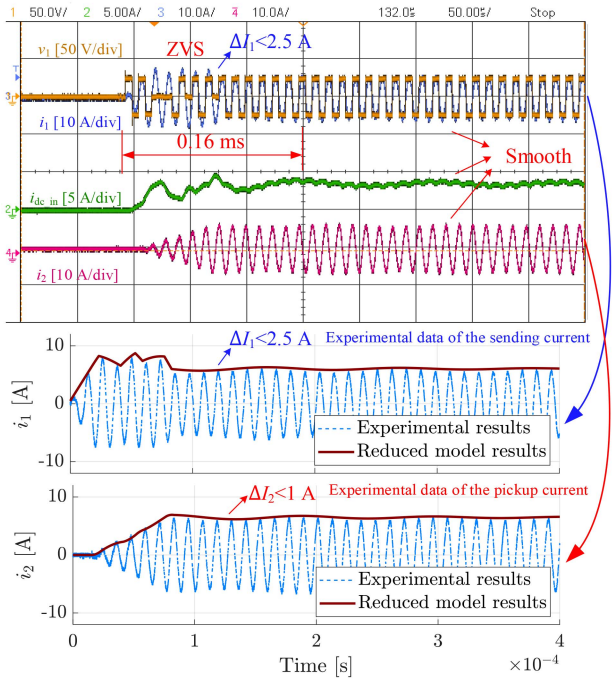

Fig. 14. Experimental results and calculated results from the reduced-order model for the proposed soft start of the WPT system with $k = 0.22$.

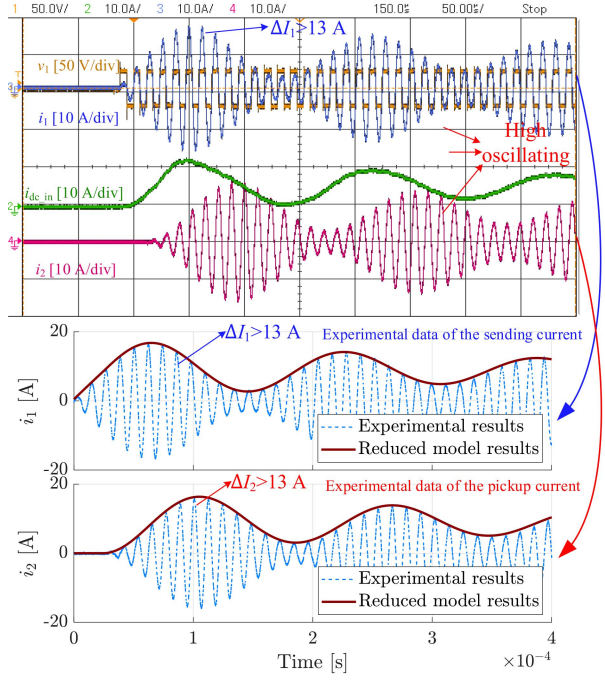

Fig. 15. Experimental results and calculated results from the reduced-order model for direct startup of the WPT system with $k = 0.145$.

Fig. 14 presents the experimental results of the soft start based on the reduced-order model design. In the initial cycles, the system operates in stage 1, as shown in Fig. 9(a), where the sending current quickly rises to the rated value while the pickup current remains at zero. The system then transitions to stage 2, as illustrated in Fig. 9(b), where the sending current fluctuates around the rated value, and the pickup current gradually increases until it reaches the rated value. Once the pickup current reaches the rated value, the system enters stage 3, where the sending side quickly stabilizes by skipping the last pulse, as analyzed in (24). Compared to the direct start, the sending current ripple of the soft-start system is reduced from 9 A to 2.5 A, while the pickup current ripple decreases from approximately 9 A to 1 A. Moreover, the input dc-side current rarely exceeds the rated value. The entire soft-start process is smooth and concludes within 0.16 ms. Furthermore, the system maintains ZVS throughout the process, as it only skips pulses without altering the phase and affecting the input impedance angle. Figs. 15 and 16 illustrate the experimental results of the system's direct startup and the proposed soft-start method under low coupling conditions ($k = 0.145$). The reduced-order model demonstrates high accuracy, closely matching the circuit model. Moreover, the current ripple in the soft-start system is significantly reduced, with the pickup-side ac current ripple decreasing from 13 A to below 1 A. The entire soft-start process is completed within 0.3 ms, even under low coupling conditions. Figs. 17 and 18 present results for different load voltages. Similarly, the reduced-order model maintains excellent accuracy while the proposed system completes the soft-start within 0.3 ms.

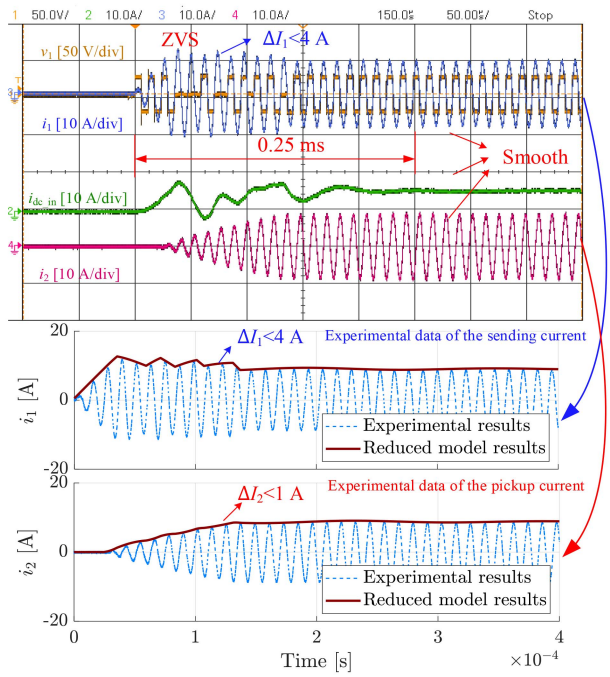

Fig. 16. Experimental results and calculated results from the reduced-order model for the proposed soft start of the WPT system with $k = 0.145$.

Figs. 19 and 20 present the experimental results for average pulse-skipping modulation and refined pulse-skipping modulation based on the reduced-order model. When the frequency of the skip pulse matches the natural frequency of the system, oscillations occur, as shown in Fig. 19 [10]. The continuous pulse density of average pulse-skipping modulation inevitably

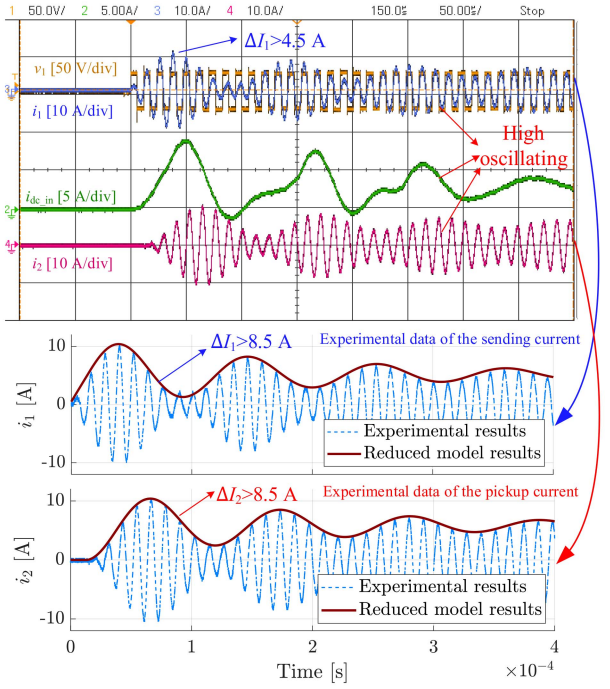

Fig. 17. Experimental results and calculated results from the reduced-order model for direct startup of the WPT system with $k = 0.22$ and $V_{\mathrm{dc\_out}} = 20$ V.

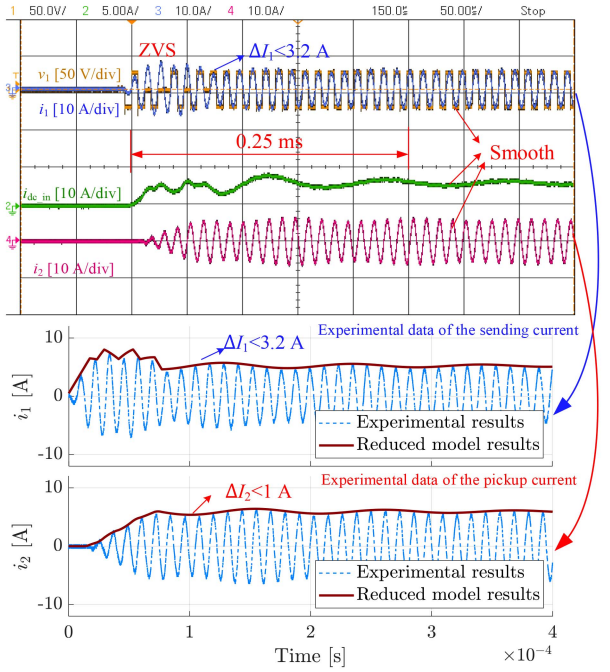

Fig. 18. Experimental results and calculated results from the reduced-order model for the proposed soft start of the WPT system with $k = 0.22$ and $V_{\mathrm{dc\_out}} = 20$ V.

leads to similar situations and sustained oscillations. When the output pulse patterns are refined using the reduced-order model, the experimental results are displayed in Fig. 20. According to (24) and the analysis of the reduced-order model, the refined pulse skips when I_2 rises and approaches the rated value. This

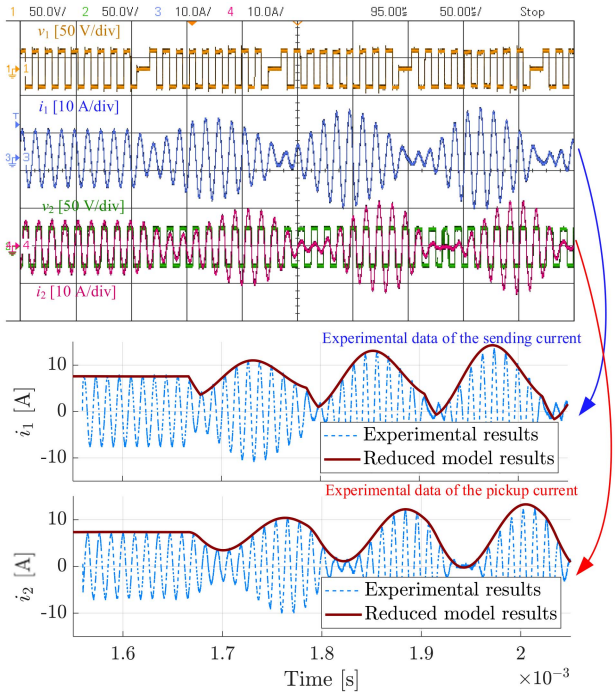

Fig. 19. Experimental results and calculated results from the reduced-order model for average pulse-skipping modulation results with $k = 0.195$ and $d = 0.9$, resulting in dc–dc efficiency $\eta_{\mathrm{dc-dc}} = 91.78\%$.

refinement significantly reduces output current and power ripples compared to average pulse-skipping modulation in Fig. 19. It is noteworthy that the system still exhibits a small residual current ripple that cannot be completely eliminated, because the two conditions in (24) cannot be satisfied exactly and can only be approached. Given the same pulse density, the output power remains quite similar in both cases. However, because of the lower current ripples (which reduce conduction losses) and maintained ZVS, the system efficiency using the proposed method is approximately 2% higher than that achieved with average pulse skipping in the worst-case scenario discussed. The reduced-order model closely aligns with the experimental results, though slight deviations arise during significant oscillations due to current distortion. Overall, this refinement shows potential for integration with the modulator to minimize output ripple across various pulse densities and operating conditions.

The analysis and experimental results confirm the applicability and accuracy of the reduced-order model for analyzing pulse skipping. This model can be used to design the proposed pulse-skipping soft-start strategy, low-ripple pulse-skipping modulations, and other scenarios requiring pulse skipping analysis. Additionally, it can facilitate conventional dynamic analysis and the design of model-based controllers [32], [33], [34]. Its verified accuracy and simplicity significantly reduce the computational burden on controllers while maintaining accuracy in dynamic and stability analyses. In this article, the SS-compensated WPT system is selected as the primary example due to its widespread adoption in various practical applications. In fact, the general applicability of the present reduced-order modeling approach

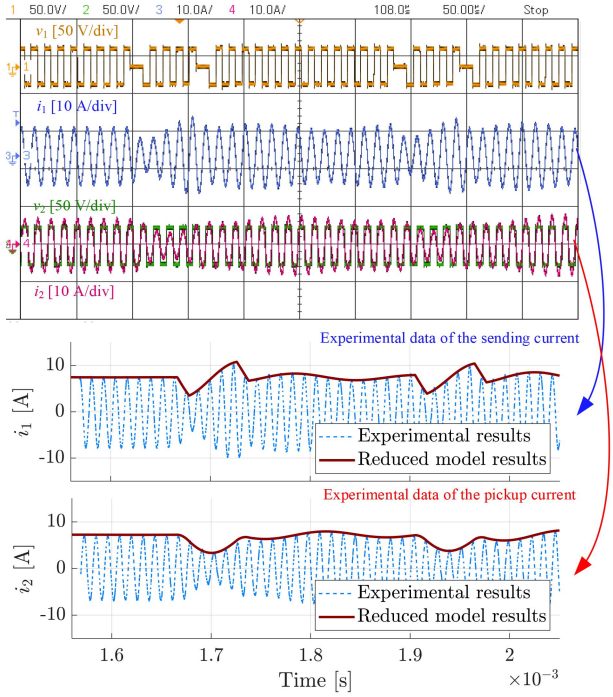

Fig. 20. Experimental results for the refined pulse-skipping modulation pattern with $k = 0.195$ and $d = 0.9$ based on reduced-order model, resulting in dc–dc efficiency $\eta_{\mathrm{dc-dc}} = 93.97\%$.

is valid for any dynamic system with an established model, regardless of the specific WPT topology or application domain. Furthermore, the proposed pulse skipping strategy for soft startup can be adapted to other compensation configurations, such as SP-compensated WPT systems. Specific implementation details for different compensation networks may warrant further investigation in future studies.

VII. Conclusion

This article presents a new reduced-order model for analyzing pulse skipping in WPT systems that is achieved through balanced truncation. The model enables the computation of high-precision ac current envelopes, facilitating a comprehensive dynamic analysis of pulse skipping. Two case studies are explored using this model. First, a pulse-skipping-based fast soft-start strategy is proposed to significantly reduce the current ripple during startup transient while ensuring ZVS throughout the process. Second, the reduced-order model is utilized to refine pulse skipping modulation to achieve minimal output current and power ripples. Importantly, the derived reduced-order model can also be applied to the dynamic analysis of other scenarios in WPT systems, such as the design of model-based controllers, to significantly reduce computational burden and simplify the analysis process. Experimental results validate the accuracy of the presented reduced-order model, as well as the effectiveness of the proposed soft start strategy and pulse skipping pattern refinement.

Acknowledgment

The authors would like to thank Dr. J. A. Suul and Dr. G. Guidi of SINTEF Energy Research for the useful discussions on the reduced-order model of WPT systems.

References

[1] S.-Y. R. Hui, Y. Yang, and C. Zhang, "Wireless power transfer: A paradigm shift for the next generation," *IEEE J. Emerg. Sel. Topics Power Electron.*, vol. 11, no. 3, pp. 2412–2427, Jun. 2023.

[2] G. A. Covic and J. T. Boys, "Modern trends in inductive power transfer for transportation applications," *IEEE J. Emerg. Sel. Topics Power Electron.*, vol. 1, no. 1, pp. 28–41, Mar. 2013.

[3] K. Agarwal, R. Jegadeesan, Y.-X. Guo, and N. V. Thakor, "Wireless power transfer strategies for implantable bioelectronics," *IEEE Rev. Biomed. Eng.*, vol. 10, pp. 136–161, 2017.

[4] G. Guidi, J. A. Suul, F. Jenset, and I. Sorfonn, "Wireless charging for ships: High-power inductive charging for battery electric and plug-in hybrid vessels," *IEEE Electr. Mag.*, vol. 5, no. 3, pp. 22–32, Sep. 2017.

[5] J. H. Kim et al., "Development of 1-MW inductive power transfer system for a high-speed train," *IEEE Trans. Ind. Electron.*, vol. 62, no. 10, pp. 6242–6250, Oct. 2015.

[6] H. Li, J. Li, K. Wang, W. Chen, and X. Yang, "A maximum efficiency point tracking control scheme for wireless power transfer systems using magnetic resonant coupling," *IEEE Trans. Power Electron.*, vol. 30, no. 7, pp. 3998–4008, Jul. 2015.

[7] Y. Jiang, L. Wang, Y. Wang, J. Liu, M. Wu, and G. Ning, "Analysis, design, and implementation of WPT system for EV's battery charging based on optimal operation frequency range," *IEEE Trans. Power Electron.*, vol. 34, no. 7, pp. 6890–6905, Jul. 2019.

[8] G. Guidi and J. A. Suul, "Minimizing converter requirements of inductive power transfer systems with constant voltage load and variable coupling conditions," *IEEE Trans. Ind. Electron.*, vol. 63, no. 11, pp. 6835–6844, Nov. 2016.

[9] Y. Zhang, K. Chen, F. He, Z. Zhao, T. Lu, and L. Yuan, "Closed-form oriented modeling and analysis of wireless power transfer system with constant-voltage source and load," *IEEE Trans. Ind. Electron.*, vol. 31, no. 5, pp. 3472–3481, May 2016.

[10] J. Zhou, G. Guidi, K. Ljøkelsøy, and J. A. Suul, "Evaluation and suppression of oscillations in inductive power transfer systems with constant voltage load and pulse skipping modulation," *IEEE Trans. Power Electron.*, vol. 38, no. 8, pp. 10412–10425, Aug. 2023.

[11] H. Li, J. Fang, S. Chen, K. Wang, and Y. Tang, "Pulse density modulation for maximum efficiency point tracking of wireless power transfer systems," *IEEE Trans. Power Electron.*, vol. 33, no. 6, pp. 5492–5501, Jun. 2018.

[12] X. Sheng, L. Shi, and M. Fan, "An improved pulse density modulation of high-frequency inverter in ICPT system," *IEEE Trans. Ind. Electron.*, vol. 68, no. 9, pp. 8017–8027, Sep. 2021.

[13] V. Yenil and S. Cetin, "An improved pulse density modulation control for secondary side controlled wireless power transfer system using LCC-S compensation," *IEEE Trans. Ind. Electron.*, vol. 69, no. 12, pp. 12762–12772, Dec. 2022.

[14] J. Zhou, G. Guidi, S. Chen, Y. Tang, and J. A. Suul, "Conditional pulse density modulation for inductive power transfer Systems," *IEEE Trans. Power Electron.*, vol. 39, no. 1, pp. 88–93, Jan. 2024.

[15] W. Zhong and S. Y. R. Hui, "Maximum energy efficiency operation of series-series resonant wireless power transfer systems using on–off keying modulation," *IEEE Trans. Power Electron.*, vol. 33, no. 4, pp. 3595–3603, Apr. 2018.

[16] S. Chen, H. Li, and Y. Tang, "Extending the operating region of inductive power transfer systems through dual-side cooperative control," *IEEE Trans. Ind. Electron.*, vol. 67, no. 11, pp. 9302–9312, Nov. 2020.

[17] W. Zhong, H. Li, S. Y. Hui, and M. D. Xu, "Current overshoot suppression of wireless power transfer systems with on-off keying modulation," *IEEE Trans. Power Electron.*, vol. 36, no. 3, pp. 2676–2684, Mar. 2021.

[18] A. K. Swain, M. J. Neath, U. K. Madawala, and D. J. Thrimawithana, "A dynamic multivariable state-space model for bidirectional inductive power transfer systems," *IEEE Trans. Power Electron.*, vol. 27, no. 11, pp. 4772–4780, Nov. 2012.

[19] S. Lee, B. Choi, and C. T. Rim, "Dynamics characterization of the inductive power transfer system for online electric vehicles by laplace phasor transform," *IEEE Trans. Power Electron.*, vol. 28, no. 12, pp. 5902–5909, Dec. 2013.
[20] H. Hao, G. A. Covic, and J. T. Boys, "An approximate dynamic model of LCL- T-based inductive power transfer power supplies," *IEEE Trans. Power Electron.*, vol. 29, no. 10, pp. 5554–5567, Oct. 2014.
[21] E. Torsgård, G. Guidi, and J. A. Suul, "Small-signal state-space analysis of inductive battery charging system in off-resonant operation," in *Proc. 20th Workshop Control Model. Power Electron.*, Toronto, ON, Canada, 2019, pp. 1–8.
[22] Z. U. Zahid et al., "Modeling and control of seriesseries compensated inductive power transfer system," *IEEE Trans. Emerg. Sel. Topics Power Electron.*, vol. 3, no. 1, pp. 111–123, Mar. 2015.
[23] H. Li, J. Fang, and Y. Tang, "Dynamic phasor-based reduced-order models of wireless power transfer systems," *IEEE Trans. Power Electron*, vol. 34, no. 11, pp. 11361–11370, Nov. 2019.
[24] F. Chen, Z. Deng, H. Hu, and Y. Sun, "Dynamic reduced-order modeling of wireless power transfer systems via polynomial approximation," *IEEE Trans. Power Electron.*, vol. 37, no. 7, pp. 7540–7547, Jul. 2022.
[25] W. Shi, J. Dong, T. B. Soeiro, J. Deng, C. Riekerk, and P. Bauer, "Continuous reduced-order dynamic model based on energy balancing for inductive power transfer systems," *IEEE Trans. Power Electron.*, vol. 37, no. 8, pp. 9959–9971, Aug. 2022.
[26] K. K. Prasad and V. Agarwal, "A novel frequency modulation technique to minimize the start-up transients in dynamic wireless charging systems for electric vehicles," in *Proc. IEEE Wireless Power Week*, 2022, pp. 834–838.
[27] J. Zhou, C. Q. Jiang, T. Ma, G. Guidi, X. Zhang, and J. A. Suul, "Comprehensive analysis of bifurcation and frequency splitting phenomena in inductive battery charging systems," *IEEE Trans. Power Electron.*, vol. 39, no. 11, pp. 15329–15341, Nov. 2024.
[28] S. P. Boyd, L. Ghaoui, E. Feron, and V. Balakrishnan, *Linear Matrix Inequalities in Systems and Control Theory*. Philadelphia, PA, USA, SIAM, 1994.
[29] S. Gugercin and A. C. Antoulas, "A survey of model reduction by balanced truncation and some new results," *Int. J. Control*, vol. 77, no. 8, pp. 748–766, 2004.
[30] K. Fernando and H. Nicholson, "Singular perturbational model reduction of balanced systems," *IEEE Trans. Autom. Control*, vol. 27, no. 2, pp. 466–468, Apr. 1982.
[31] T. Hamada, T. Fujita, and H. Fujimoto, "Fast start-up control of both-side current without overshoot focusing on rectification timing for dynamic wireless power transfer systems," *IEEE J. Emerg. Sel. Topics Ind. Electron.*, vol. 5, no. 3, pp. 1039–1047, Jul. 2024.
[32] C. Qi, Z. Lang, L. Su, X. Chen, and H. Miao, "Finite-control-set model predictive control for a wireless power transfer system," in *Proc. IEEE Int. Symp. Predictive Control Elect. Drives Power Electron.*, Quanzhou, China, 2019, pp. 1–5.
[33] J. Zhou, S. Chen, G. Guidi, Y. Tang, and J. A. Suul, "Dynamic improvement of sub-resonant frequency control for inductive power transfer systems by coupling estimation and sending-side gain-scheduled control," *IEEE Trans. Ind. Appl.*, vol. 60, no. 2, pp. 3734–3745, Mar./Apr. 2024.
[34] Z. Ye and K. W. E. Cheng, "Design and validation of a multioutput wireless power transfer system using MPC controller," *IEEE Trans. Power Electron*, vol. 39, no. 12, pp. 16065–16077, Dec. 2024.

Jiayu Zhou received the B.Eng. and M.S. degrees in electrical engineering from Beijing Jiaotong University, Beijing, China, in 2016 and 2019, respectively, and the Ph.D. degree in engineering cybernetics from the Norwegian University of Science and Technology, Trondheim, Norway, in 2023.

He is currently a Postdoctoral Research Fellow with City University of Hong Kong. His research interests include wireless power transfer and power converters for renewable energy systems.

Jiayang Wu (Member, IEEE) received the B.Eng. degree in electrical information engineering from Zhejiang University, Hangzhou, China, in 2017, and the Ph.D. degree in electrical and electronic engineering from The University of Hong Kong, Hong Kong, in 2022.

She was a Research Fellow with the School of Electrical and Electronic Engineering, Nanyang Technological University, Singapore in 2023. Following this role, she held the position of a Research Assistant Professor with the Department of Electrical and Electronic Engineering, The University of Hong Kong, Hong Kong, in 2024. She is currently a Research Assistant Professor with the Department of Electrical Engineering, City University of Hong Kong, Hong Kong. She also holds two Chinese patents and one U.S. patent. Her current research interests include wireless power transfer, electric vehicle charging, resonant converters, and renewable energy.

Dr. Wu was a recipient of the Best Paper Award (Second Place) of IEEE TRANSACTIONS ON POWER ELECTRONICS in 2019 and 2023, and the Best Presentation Award of the IEEE Applied Power Electronics Conference and Exposition in 2024.

C. Q. Jiang (Senior Member, IEEE) received the B.Eng. and M.Eng. degrees (first class hons.) in electrical engineering and automation from Wuhan University, Wuhan, China, in 2012 and 2015, respectively, and the Ph.D. degree in electrical and electronic engineering from The University of Hong Kong, Hong Kong, in 2019.

He is currently an Associate Professor with the Department of Electrical Engineering, Faculty Member with the State Key Laboratory of Terahertz and Millimeter Waves, City University of Hong Kong, Hong Kong. Since 2021, he has also been with Clare Hall, University of Cambridge. From 2019 to 2021, he was a Postdoctoral Research Associate with the University of Cambridge, Cambridge, U.K. In 2019, he was a Visiting Researcher with the Nanyang Technological University, Singapore. His research interests include power electronics, wireless power transfer techniques, electric machines and drives, and electric vehicle technologies.

Dr. Jiang was a recipient of the CENG Research Excellence Award, the Gold Medal at the Silicon Valley International Invention Festival, the Gold Medals with Congratulations of the Jury in International Exhibition of Inventions of Geneva, the Winner of CAPE Acorn Blue Sky Research Award with the University of Cambridge, the Gold Medal in Third Asia Exhibition of Innovations and Inventions, the Silver Award and Bronze Award in Shenzhen Qianhai Youth Innovation and Entrepreneurship Competition, and the First Prize in the Interdisciplinary Research Competition at the University of Hong Kong. He is currently an Associate Editor of IET Renewable Power Generation and a Guest Editor of IEEE OPEN JOURNAL OF VEHICULAR TECHNOLOGY and *IEEE Transactions on Power Electronics Letters*.

Xiaosheng Wang received the B.Eng. degree in electrical engineering and automation from Henan Polytechnic University, Jiaozuo, China, in 2016, the M.Sc. degree in new energy science and engineering from Huazhong University of Science and Technology, Wuhan, China, in 2019, and the Ph.D. degree in electrical engineering with the Department of Electrical Engineering, City University of Hong Kong, Hong Kong, in 2025.

He is a Postdoctoral Fellow with the Department of Electrical Engineering, City University of Hong Kong. His research interests include wireless power transfer, motor control, and power quality.

Siew-Chong Tan (Fellow, IEEE) received the B.Eng. (hons.) and M.Eng. degrees in electrical and computer engineering from the National University of Singapore, Singapore, in 2000 and 2002, respectively, and the Ph.D. degree in electronic and information engineering from The Hong Kong Polytechnic University, Hong Kong, in 2005.

He is currently a Chair Professor with the Department of Electrical Engineering, City University of Hong Kong, Hong Kong. He was a Visiting Scholar with Grainger Center for Electric Machinery and Electromechanics, University of Illinois at Urbana-Champaign, Champaign, from Sep. to Oct. 2009, and an Invited Academic Visitor of Huazhong University of Science and Technology, Wuhan, China, in 2011. His research interests include power electronics and control, LED lightings, smart grids, and clean energy technologies.

Shu-Yuen Ron Hui (Fellow, IEEE) received the B.Sc. (Eng) hons. in electrical and electronic engineering with the University of Birmingham, Birmingham, U.K., in 1984, and the D.I.C. and Ph.D. degrees in electrical engineering from Imperial College London, London, U.K., in 1987.

He is currently a Chair Professor of Power Electronics with the City University of Hong Kong, and Imperial College London. He held academic positions with the University of Nottingham, and University of Sydney, and endowed professorship with the University of Hong Kong. He has authored or coauthored more than 500 research papers including 330 refereed journal publications. According to IEEE Xplore, his patent citations exceed 1260. Over 125 of his patents have been adopted by industry worldwide. His research interests include power electronics, wireless power, sustainable lighting, and smart grid.

Dr. Hui inventions on wireless charging platform technology underpin key dimensions of Qi, the world's first wireless power standard, with freedom of positioning and localized charging features for wireless charging of consumer electronics. He also developed the Photo-Electro-Thermal Theory for LED Systems and Electric Spring technology for smart grid. He was the recepinet of the IEEE Rudolf Chope R&D Award and the IET Achievement Medal (The Crompton Medal) in 2010, IEEE William E. Newell Power Electronics Award in 2015, and the IET JJ Thomson Medal in 2024. He is a Fellow of the Australian Academy of Technology and Engineering, US National Academy of Inventors, and Royal Academy of Engineering, U.K.